PERIODICO di MINERALOGIA
established in 1930

DIPARTIMENTO
DI SCIENZE DELLA TERRA

SAPIENZA
UNIVERSITÀ DI ROMA

An International Journal of
Mineralogy, Crystallography, Geochemistry,
Ore Deposits, Petrology, Volcanology
and applied topics on Environment, Archaeometry and Cultural Heritage

Mineralogical and micromorphological characteristics of the limescale in a kettle: Insights into polymorph formation

Muhsin Eren [1,*], Selahattin Kadir [2,†], Meryem Yeşilot Kaplan [3]

[1] Department of Geological Engineering, Mersin University, Mersin, Turkey
[2] Department of Geological Engineering, Eskişehir Osmangazi University, Eskişehir, Turkey,
† Deceased
[3] Department of Petroleum and Natural Gas Engineering Faculty, İskenderun Technical University, Hatay, Turkey

ARTICLE INFO

Submitted: October 2025
Accepted: August 2026
Available on line: September 2026

* Corresponding author:
meryem.yesilotkaplan@iste.edu.tr

Doi: 10.13133/2239-1002/19108

How to cite this article:
Eren M. et al. (2026)
Period. Mineral. 95, 281-291

ABSTRACT

This study presents an integrated mineralogical, micromorphological, spectroscopic, and geochemical characterization of kettle limescale formed from hard tap water in Mersin, southern Turkey. Petrographic microscopy, X-ray diffraction, Fourier-transform infrared spectroscopy, scanning electron microscopy with energy-dispersive X-ray spectroscopy, inductively coupled plasma mass spectrometry, Raman spectroscopy, and ion chromatography were used to characterize the limescale and source water. The limescale consists predominantly of aragonite and calcite, with aragonite as the dominant crystalline phase. Scanning electron microscopy reveals pseudo-hexagonal prismatic, needle-like, and rhombohedral crystals, together with rosette-, cauliflower-, and hexagonal plate-like aggregates. Integrated morphological, spectroscopic, and compositional data indicate that needle-like and rhombohedral crystals are predominantly calcitic, whereas pseudo-hexagonal prisms and irregular morphologies are predominantly aragonitic. The irregular morphologies, together with poorly ordered carbonate material, are enriched in magnesium and silicon but depleted in calcium, representing compositionally distinct late-stage precipitates. These findings support a multistage precipitation model involving initial calcite nucleation, subsequent aragonite growth during boiling, and late-stage precipitation of Mg–Si-rich, poorly ordered carbonate material.

Keywords: kettle limescale; micromorphology; $CaCO_3$ polymorphs; mineralogy; scale-water chemistry; Mersin (Turkey).

INTRODUCTION

Limescale, composed predominantly of calcium carbonate ($CaCO_3$), commonly accumulates in kettles and other household appliances when hard water is heated. Thermal decomposition of dissolved bicarbonate increases carbonate supersaturation, leading to rapid $CaCO_3$ precipitation, often accompanied by minor Mg-bearing phases. Such deposits reduce heating efficiency, shorten appliance lifespan, increase energy consumption, and impair water quality (Abdelghani et al., 2018; Al-Gailani et al., 2022).

Although carbonate scaling in industrial and domestic water systems has been extensively investigated, the mineralogical evolution and micromorphological diversity of kettle limescale remain insufficiently characterized. Butler (1975) distinguished two mineralogical zones in kettle deposits: an upper layer of aragonite and Mg-calcite and a lower zone dominated by Mg-calcite with minor amorphous silica. Later studies in household water systems documented similar carbonate accumulations (Hafid et al., 2015; Belattar et al., 2016). Nevertheless, relatively few studies have combined mineralogical,

spectroscopic, micromorphological, and geochemical approaches to investigate the mechanisms controlling carbonate polymorphism and crystal morphology during kettle limescale formation.

The present study provides an integrated mineralogical, micromorphological, spectroscopic, and geochemical characterization of kettle limescale using XRD, FTIR, Raman spectroscopy, SEM-EDX, ICP-MS, and ion chromatography. Tap water, supplied from the Berdan Dam to Mersin city, was also analyzed to evaluate the relationship between water chemistry and carbonate precipitation. The Berdan Dam catchment comprises ophiolitic, evaporitic, and carbonate lithologies (Yetiş et al., 1995; Kapur et al., 2025), which contribute Ca, Mg, Si, Al, and trace elements to the water. By integrating mineralogical, spectroscopic, morphological, and geochemical evidence, this study aims to improve understanding of the factors controlling carbonate polymorphism, crystal morphology, and elemental partitioning during low-temperature limescale formation.

MATERIALS AND METHODS

Flaky limescale samples were collected by gently scraping the interior base of a stainless-steel kettle that had been repeatedly used for boiling tap water. A small volume of water was added to the dry-heated kettle during sampling to facilitate the detachment of flakes. A tap water sample from the same supply was collected for chemical analysis.

Two thin sections of the limescale were prepared and examined under a polarizing microscope to identify textural and microstructural features.

X-ray diffraction (XRD) analysis was performed on powdered samples (<63 μm) using a Rigaku D/Max-2200 Ultima PC diffractometer equipped with Cu Kα radiation (λ=1.5406 Å) and operated at 45 kV and 40 mA. Data were collected over a 2θ range of 5-70° using a step size of 0.02° and a scanning speed of 1° min^{-1}. The diffraction patterns were interpreted manually from the relative positions and intensities of the reflections, following the procedures described by Brindley (1980) and Moore and Reynolds (1989).

Fourier-transform infrared spectroscopy (FTIR) analysis was conducted on finely ground powders (<2 μm) mixed with KBr at a ratio of 1:100 and pressed into pellets. Spectra were recorded using a PerkinElmer Spectrum 100 FT-IR spectrometer in the range of 4000-400 cm^{-1}, with a resolution of 4 cm^{-1} and 32 scans. Baseline corrections and band assignments were performed using Spectrum software (PerkinElmer) following the reference data of Van der Marel and Beutelspacher (1976).

The micromorphology and microchemical composition of the carbonate polymorphs were investigated by scanning electron microscopy (SEM) with energy-dispersive X-ray spectroscopy (EDX). Analyses were performed using a Hitachi Regulus 8230 FE-SEM equipped with an Oxford Instruments ULTIM EXTREME EDX detector. To ensure surface conductivity and minimize charging, the samples were coated with a thin layer of gold (~350 Å) using a Quorum SC7640 sputter coater.

Raman spectroscopy was performed using a Renishaw inVia Raman microscope with a 532 nm laser and a spot size of approximately 1 μm. The laser was focused on the sample through a petrographic microscope equipped with a 50× objective. Spectra were collected over accumulations of 10s each, using 10% of the total laser power (50 mW) to avoid damaging the sample. Baseline correction was performed using WiRE 5.5 software (Renishaw plc., Wotton-under-Edge, UK) before spectral interpretation. Peak fitting was not performed because overlapping carbonate bands and the mixed-phase character of the spectra precluded robust quantitative deconvolution. Raman spectra were interpreted qualitatively using the characteristic carbonate bands described by Kontoyannis and Vagenas (2000) together with the updated carbonate Raman assignments of Alves et al. (2023). Because the analyzed domains commonly consisted of intergrown carbonate phases and the characteristic aragonite band near 700 cm^{-1} was not consistently resolved, no quantitative calcite/aragonite ratios were calculated.

Major and trace element concentrations in both limescale and water were determined by inductively coupled plasma mass spectrometry (ICP-MS, Agilent 7900). Cation and anion concentrations in the tap water were analyzed using ion chromatography (IC, Thermo Scientific Dionex ICS-5000). The analyzed elements and ions included Na, K, Mg, Ca, Sr, Fe, Mn, Ba, F^-, Cl^-, NO_3^-, and SO_4^{2-}. The pH and electrical conductivity of the tap water were also measured to characterize its hydrochemical properties better.

The chemical analyses, including ICP-MS, IC, and measurements of pH and electrical conductivity, were performed at Mersin University (MEİTAM), while the mineralogical (XRD, FTIR) and micromorphological (SEM-EDX) analyses were conducted at Eskişehir Osmangazi University under standardized quality-control conditions. The Raman spectroscopy was carried out at Çukurova University (CU-CRL).

The total hardness of the tap water was calculated as $CaCO_3$ (ppm) based on the measured concentrations of Ca^{2+} and Mg^{2+}. The calculation follows the standard conversion approach outlined by Gray (2008):

$$\text{Hardness (ppm as } CaCO_3) = 2.497 \cdot [Ca^{2+}] + 4.118 \cdot [Mg^{2+}]$$

where $[Ca^{2+}]$ and $[Mg^{2+}]$ are in ppm. These coefficients

are derived from the ratio of the equivalent weight of $CaCO_3$ (50) to the equivalent weights of Ca^{2+} (20.04) and Mg^{2+} (12.16), respectively.

RESULTS

Macroscopic and microscopic features

The limescale coating at the bottom of the kettle is white, finely crystalline, and approximately 1-1.5 mm thick. Its upper surface is irregular and marked by small, hollow, cone-shaped structures (Figure 1a), whereas the lower surface is smooth. Microscopically, it displays a dark brown micritic texture with circular cavities interpreted as micro-cone traces (Figure 1b).

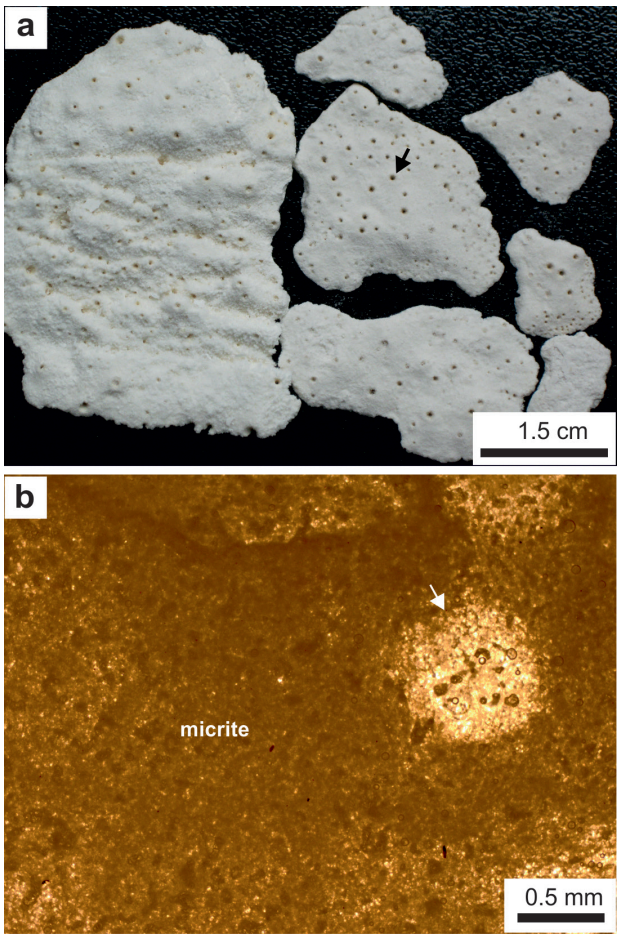

Figure 1. Photographs showing: a) Flake-like fragments of the limescale removed from the kettle, characterized by a milky white color and finely crystalline structure with micro-cones, each featuring a central hole (arrow); b) Microphotograph of the limescale, displaying a micritic texture and remnants of the micro-cones (arrow).

XRD analysis

XRD confirms aragonite and calcite as the dominant crystalline phases. Characteristic reflections of aragonite occur at 4.21, 3.40, and 3.27 Å, whereas calcite is identified by peaks at 3.03, 2.82, and 2.48 Å (Figure 2). The diffraction pattern confirms the coexistence of both polymorphs; however, no quantitative phase analysis was performed, and therefore their relative abundances cannot be determined from the XRD data alone.

Infrared spectra

The FTIR spectrum (Figure 3) exhibits the characteristic absorption bands of aragonite (1472, 1083, 1002, 855, 713, and 700 cm^{-1}) and calcite (1790, 1422, 1060, 874, and 713 cm^{-1}). Sharp bands indicate high crystallinity, consistent with the crystalline carbonate phases identified by XRD.

SEM-EDX analysis

SEM-EDX analysis reveals a wide variety of carbonate crystal morphologies within the kettle limescale (Figure 4), each with characteristic elemental compositions (Table 1). Elongated pseudo-hexagonal prismatic crystals with smooth faces and tapered terminal tips are the dominant morphology (Figure 4 a-d). These prisms reach up to 90 µm in length and approximately 10 µm in diameter and commonly form loosely interconnected networks. Their elemental compositions are characterized by Ca as the dominant element, with generally low Mg contents (<2 wt%) and detectable Sr enrichment (Table 1).

Rod-shaped needles are also abundant throughout the deposits. They are typically 1-2 µm wide and occur both as isolated crystals and in close association with the pseudo-hexagonal prisms, either attached to their surfaces or enclosed within them (Figure 4 b-d). Small rhombohedral crystals, generally less than 10 µm in size, are likewise common and frequently occur on the surfaces of the prismatic crystals, locally displaying intergrowth relationships (Figure 4 b,d). The needle- and rhombohedron-bearing domains exhibit Ca-rich and Mg-poor compositions broadly comparable to those of the pseudo-hexagonal prisms, with only minor variations in Mg, Al, and Si contents (Table 1). Consequently, the EDX data alone are insufficient to distinguish individual carbonate polymorphs. Accordingly, the mineralogical interpretation of these morphologies relies on their crystal habits together with the complementary evidence from XRD, FTIR, and Raman spectroscopy.

Irregular, more complex morphologies are represented by rosette-like aggregates (Figure 4e), hexagonal plates (Figure 4 f,g), cauliflower-like aggregates (Figure 4h), and poorly ordered carbonate material (POC). These morphologies exhibit elemental compositions distinct

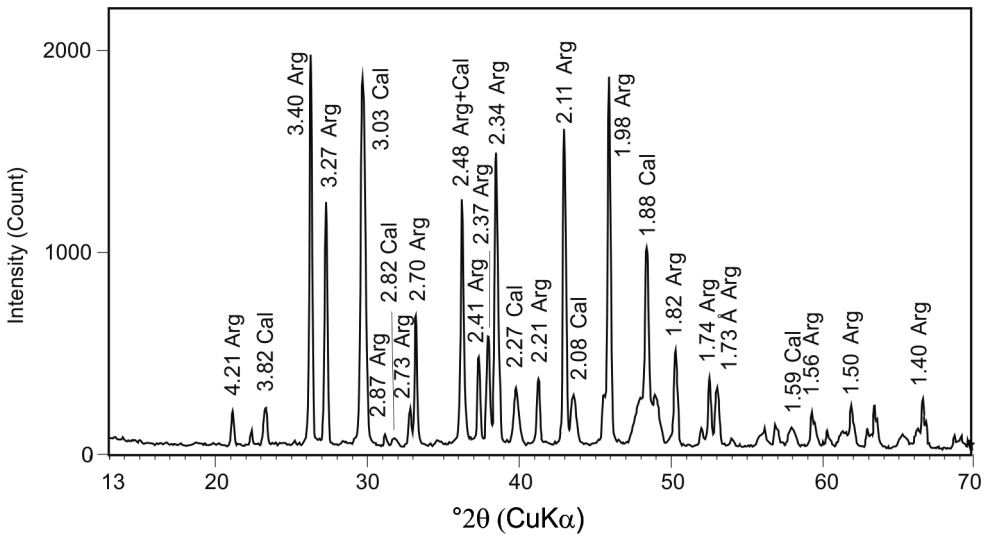

Figure 2. XRD pattern of the kettle limescale, showing the characteristic basal reflections of aragonite (Arg) and calcite (Cal) as the dominant mineral phases.

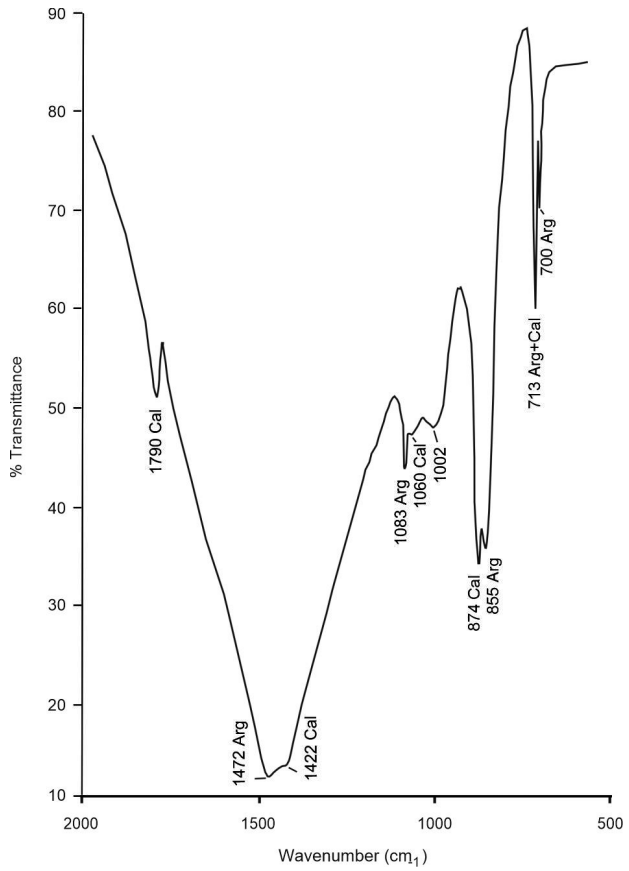

Figure 3. FTIR spectra of the limescale, highlighting distinct absorption bands characteristic of aragonite (Arg) and calcite (Cal). The specific vibrational modes associated with each mineral phase are labeled, confirming the presence of both polymorphs within the sample.

from those of the crystalline carbonate morphologies. Rosette-like aggregates, approximately 1-2 μm in diameter, occur on the surfaces of both pseudo-hexagonal prisms and rhombohedral crystals, particularly in the upper part of the deposits (Figure 4e). Hexagonal plates are observed near the lower surface of the limescale and locally develop along partially dissolved prism surfaces (Figure 4 f,g). The POC forms nano-aggregates intimately associated with the hexagonal plates (Figure 4f). The cauliflower-like aggregates, measuring approximately 3-6 μm, consist of clusters of spherical nanocrystallites ranging from about 0.5 to 2 μm in diameter (Figure 4h).

These morphologies are distinguished by markedly elevated Mg (10-22 wt%) and Si (3-20 wt%) contents together with substantially lower Ca concentrations than the dominant crystalline morphologies (Table 1), indicating the presence of chemically distinct Mg-Si-rich carbonate material. The mineralogical interpretation of these morphologies is based on the integrated evaluation of the SEM-EDX observations together with the XRD, FTIR, and Raman spectroscopy results presented in the following sections.

Raman spectroscopy

All analyzed morphologies exhibit the characteristic Raman bands of carbonate minerals (Figure 5). Peak assignments follow the reference spectra of Alves et al. (2023), whereas the expected positions of the principal calcite Raman bands are consistent with the compilation of Itoh (2026). Calcite needles display bands at 1092, 711, 282, 211, and 158 cm^{-1}, whereas calcite rhombs exhibit bands at 1091, 712, 282, 212, and 157 cm^{-1}. Hexagonal prisms display bands at 1092, 709, 213, and

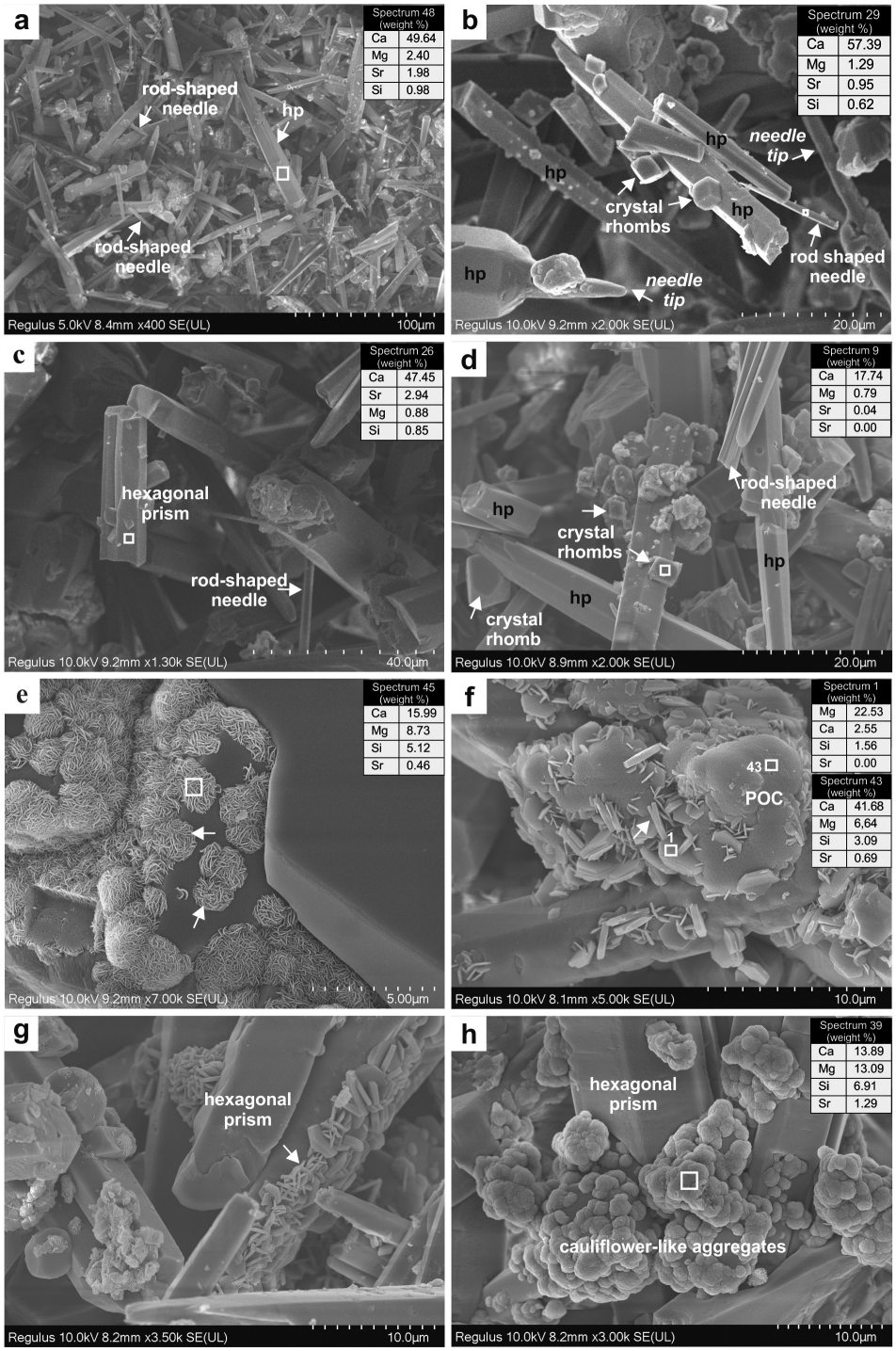

Figure 4. SEM images of the kettle limescale with corresponding EDX elemental compositions (wt%): a) Randomly oriented and loosely packed pseudo-hexagonal prismatic crystals (hp), together with rod-shaped needles. The prismatic crystals exhibit hexagonal cross-sections, smooth surfaces, and pointed terminations; b) Close-up of (a), showing pseudo-hexagonal prismatic crystals (hp) with smooth surfaces and pointed terminations (needle tips), small rhombohedral crystals on the prism surfaces, and rare rod-shaped needles; c) Close-up view of a pseudo-hexagonal prismatic crystal and a rod-shaped needle; d) Small rhombohedral crystals occurring individually or in clusters on the surfaces of the prismatic crystals (hp); e) Rosette-like aggregates (arrows); f) Hexagonal plates (arrow) partially embedded in poorly ordered carbonate material (POC); g) Hexagonal plates developing along the partially dissolved surface of a pseudo-hexagonal prismatic crystal (arrow); h) Cauliflower-like aggregates on the surfaces of the prismatic crystals. The results of the EDX analyses are shown in each image, with the analyzed area indicated by a white square.

Table 1. SEM-EDX elemental compositions (wt%) of the principal limescale morphologies observed in the kettle deposits.

Morphology	Spec. No	C	O	Mg	Al	Si	Ca	Sr
Pseudo-hexagonal prisms	1	16.14	35.59	0.44	2.24	0.36	44.99	0.24
	2	20.34	57.10	0.13	0.27	0.07	21.96	0.13
	6	14.74	26.53	0.63	2.77	1.21	53.24	0.88
	10	23.47	57.46	0.26	0.33	0.00	18.49	0.00
	17	28.40	54.61	0.00	0.47	0.06	16.34	0.12
	21	11.91	31.71	0.00	1.93	0.00	53.50	0.95
	22	6.86	13.47	0.13	3.09	0.00	75.72	0.74
	25	9.49	30.89	1.97	2.09	1.39	53.23	0.94
	26	12.71	34.60	0.88	0.56	0.85	47.45	2.94
	27	12.05	29.81	0.21	0.99	0.85	53.87	2.23
	30	11.43	31.13	1.68	2.43	0.00	53.33	0.00
	32	14.82	45.13	0.09	1.72	0.03	36.86	1.35
	37	3.04	15.74	0.30	2.33	0.38	76.32	1.89
	41	9.57	26.33	1.03	3.93	0.00	57.48	1.66
	42	5.54	20.60	1.38	1.70	0.00	70.78	0.00
	48	10.59	33.17	2.40	1.24	0.98	49.64	1.98
	Mean ± Sd	13.19 ± 6.55	33.99 ± 13.48	0.72 ± 0.76	1.76 ± 1.06	0.39 ±0.50	48.95 ± 18.26	1.00±0.92
Rod-shaped needle	11	13.68	24.55	0.20	1.61	0.18	59.71	0.07
	28	14.69	39.89	0.75	0.54	0.44	43.52	0.19
	29	12.15	26.90	1.29	0.71	0.62	57.39	0.95
	31	13.36	40.77	0.39	0.78	0.00	43.41	1.29
	Mean ± Sd	13.47±1.05	33.03±849	0.66±0.48	0.91±0.48	0.31±0.27	51.01±8.76	0.63±0.59
Rhombohedral crystals	3	11.87	33.85	1.79	0.50	0.00	51.40	0.59
	7	23.45	57.20	0.90	0.72	0.03	16.72	0.98
	9	24.67	55.67	0.70	1.18	0.00	17.74	0.04
	14	24.85	52.38	1.18	0.47	0.03	21.01	0.08
	15	17.57	45.35	1.00	0.95	0.11	35.02	0.00
	33	15.66	14.09	1.28	3.19	1.90	63.87	0.00
	Mean ± Sd	19.68±0.41	43.09±19.63	1.14±0.76	1.17±1.03	0.35±0.76	34.29±19.63	0.28±0.41
Rosette-like aggregates	8	21.20	49.37	13.50	2.94	6.73	3.63	2.62
	18	18.23	42.03	2.35	1.57	0.74	35.07	0.00
	19	26.11	48.12	2.69	1.95	0.57	20.56	0.00
	34	9.88	40.83	4.31	1.88	2.20	40.88	0.00
	45	19.76	48.51	8.73	1.42	5.12	15.99	0.46
	46	11.26	47.32	12.34	1.81	9.32	17.95	0.00
	47	13.11	51.35	16.94	1.81	9.40	7.38	0.00
	Mean ± Sd	17.08±5.89	46.79±3.89	8.69±5.77	1.91±0.49	4.87±3.80	20.21±13.61	0.44±0.98
Cauliflower-like aggregates	20	20.85	28.86	10.66	2.63	11.68	23.96	1.36
	23	17.28	50.31	11.39	1.19	6.23	13.60	0.00
	24	14.05	53.81	16.34	1.47	8.73	5.50	0.10
	39	13.52	49.90	13.09	1.41	6.91	13.89	1.29
	41	9.57	26.33	1.03	3.93	0.00	57.48	1.66
	43	13.80	32.08	6.64	2.02	3.09	41.68	0.69
	44	14.96	18.85	12.03	1.2	20.15	28.97	3.84
	C4	15.56	57.11	15.18	0.73	7.98	3.43	nd
	Mean ± Sd	14.95±3.25	39.66±14.68	10.80±4.92	1.82±1.03	8.10±6.02	23.56±18.64	1.12±1.30
Hexagonal plates	1*	6.29	28.14	22.53	0.99	1.56	2.55	nd

*The hexagonal plate shows a high Au value (37.93 wt%), which results from the Au-coating applied during analysis (see also Figure 4f); nd: not determined, Sd: standard deviation.

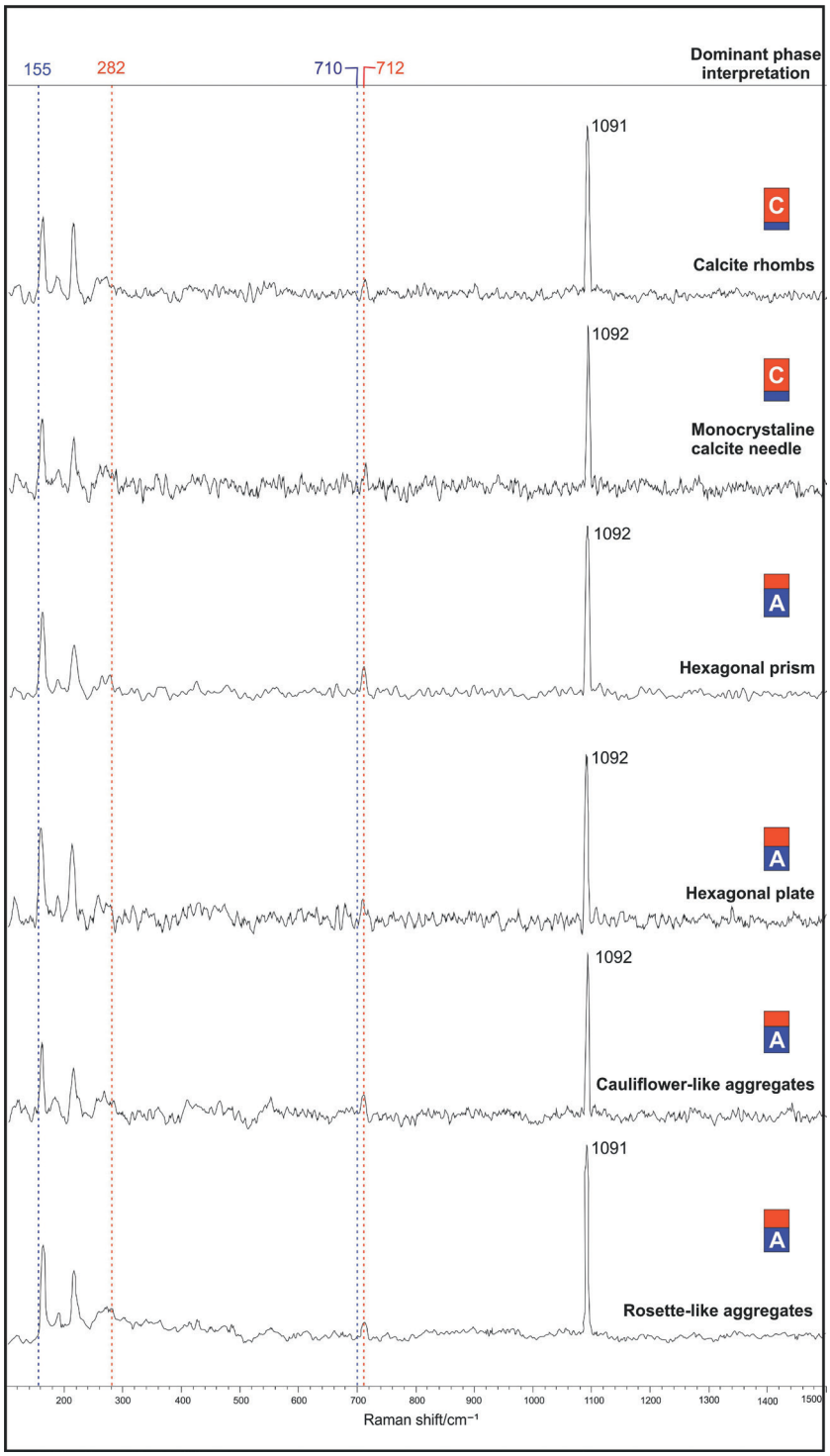

Figure 5. Raman spectra of the principal limescale morphologies, including calcite rhombs, rod-shaped needles, pseudo-hexagonal prismatic crystals, hexagonal plates, cauliflower-like aggregates, and rosette-like aggregates. Vertical dashed lines indicate the characteristic Raman bands used for qualitative comparison of the spectra. The Raman spectra confirm the coexistence of calcite and aragonite identified by XRD and FTIR but do not permit reliable quantitative estimation of calcite/aragonite proportions because several analyzed domains comprise intergrown carbonate phases. Accordingly, the spectra were interpreted qualitatively in conjunction with XRD, FTIR, SEM morphology, and EDX microchemical data. The symbols C and A indicate the dominant carbonate polymorph (calcite- or aragonite-dominant, respectively) inferred from the integrated interpretation of XRD, FTIR, Raman spectroscopy, SEM crystal morphology, and EDX microchemical data rather than from quantitative Raman phase analysis alone.

158 cm^{-1}; cauliflower-like aggregates at 1092, 711, 213, and 158 cm^{-1}; rosette-like aggregates at 1091, 708, 211, and 158 cm^{-1} and hexagonal plates at 1092, 710, 208, and 155 cm^{-1}.

Overall, the Raman spectra exhibit only subtle variations among the analyzed morphologies. Differences among the spectra are reflected primarily by variations in the relative intensities of the characteristic calcite and aragonite bands rather than by systematic shifts in peak positions. Minor variations in the ν_1 carbonate band (1091-1092 cm^{-1}) and the ν_4 bending region (708-712 cm^{-1}) were observed among the analyzed morphologies; however, these differences are small relative to the overall spectral similarity.

The Raman spectra confirm the coexistence of calcite and aragonite previously identified by XRD and FTIR. Minor differences in the relative intensities of the characteristic carbonate bands are consistent with variations in the dominant carbonate polymorph among the analyzed morphologies. Because several analyzed domains comprise intimate intergrowths of carbonate phases and the characteristic aragonite band near 700 cm^{-1} is not consistently resolved, the Raman data are interpreted qualitatively rather than quantitatively. Accordingly, the mineralogical interpretation of the analyzed morphologies is based on the integrated evaluation of Raman spectra, XRD, FTIR, SEM crystal morphology, and SEM-EDX data. This integrated interpretation indicates that the needle-like and rhombohedral crystals are predominantly calcitic, whereas the pseudo-hexagonal prisms and irregular morphologies are predominantly aragonitic.

Chemical analysis

ICP-MS and IC analyses reveal distinct compositional differences between the tap water and the kettle limescale (Tables 2 and 3). The tap water contains measurable concentrations of Si (1.67 ppm), B (49.37 ppb), Ba (13.38 ppb), P (8.24 ppb), Ni (2.60 ppb), Cr (2.58 ppb), and Zn (1.52 ppb), whereas most trace elements in the limescale are below the analytical detection limits (Table 2). Conversely, the limescale is strongly enriched in Ca (36,043 ppm), Mg (1,330 ppm), Al (491 ppm), and Si (56.98 ppm), reflecting the preferential incorporation of these elements during carbonate precipitation.

IC analysis indicates that Ca^{2+} (59.5 ppm) and Mg^{2+} (11.8 ppm) are the dominant cations, followed by Na^{+} (18.9 ppm) and K^{+} (0.62 ppm). Among the anions, SO_4^{2-} (15.9 ppm) and Cl^{-} (15.2 ppm) predominate, whereas NO_3^{-} (2.8 ppm) and F^{-} (0.1 ppm) occur at lower concentrations (Table 3). The tap water has a pH of 8.28, an electrical conductivity of 386 µS cm^{-1}, and a total hardness of 197 ppm as $CaCO_3$, indicating moderately hard water.

DISCUSSION

The mineralogical, micromorphological, and geochemical characteristics of the kettle limescale collectively indicate a multistage precipitation sequence controlled by progressive heating, evolving solution chemistry, and evaporation. The relatively high Ca and Mg concentrations in the tap water, derived from the ophiolitic, evaporitic, and carbonate lithologies of the Berdan Dam catchment (Yetiş et al., 1995; Kapur et al., 2025), together with a calculated hardness of approximately 197 ppm as $CaCO_3$ (Gray, 2008; Martínez Moya and Boluda Botella, 2021), provided favorable conditions for carbonate precipitation. Repeated boiling progressively removed dissolved CO_2, thereby increasing carbonate supersaturation and promoting sequential precipitation of $CaCO_3$ polymorphs. A comparison of the tap water and limescale compositions further demonstrates selective enrichment during this process. Compared with the tap water, the limescale is enriched in Ca, Mg, Si, and Al, whereas several trace elements detected in the water (e.g., B, Cr, Ni, Zn, and Ba) remain below detection limits in the solid phase. This compositional evolution shows that Ca was primarily incorporated into the crystalline carbonate phases, while Mg and Si became progressively more concentrated during evaporation and were preferentially incorporated into chemically distinct late-stage morphologies.

SEM observations suggest that rod-shaped needles and small rhombohedral crystals formed during the earliest stages of limescale development. The occurrence of rod-shaped needles both as isolated crystals and enclosed within elongated pseudo-hexagonal prismatic crystals, with their terminal tips locally protruding beyond the prism terminations, indicates that the needles predate prism formation and acted as substrates for subsequent crystal growth. This textural relationship is consistent with experimental studies showing that calcite is preferentially formed during the initial stages of heating, whereas increasing temperature, progressive CO_2 degassing, and increasing carbonate supersaturation promote aragonite precipitation (Wray and Daniels, 1957; Burton and Walter, 1987; Fernández-Díaz et al., 1996; De Choudens-Sánchez and González, 2009; Hanifa et al., 2025; Liendo et al., 2022).

The predominance of aragonite in the bulk limescale indicates that prolonged boiling maintained conditions favorable for continued aragonite growth throughout most of the precipitation process. This interpretation is supported by the greater abundance of aragonite identified by XRD and by the dominance of elongated pseudo-hexagonal prisms observed in the SEM images. Their smooth crystal faces, tapered terminations, and consistently low Mg contents are consistent with

Table 2. Major and trace element compositions of the source tap water and limescale as determined by ICP-MS analysis.

Elements	water	limescale
B (ppb)	49.37	<1
Na (ppm)	nd	<0.01
Mg (ppm)	nd	1330
Al (ppm)	0.06	491
Si (ppm)	1.67	56.98
P (ppb)	8.24	<1
K (ppm)	nd	<0,01
Ca (ppm)	nd	36043
Cr (ppb)	2.58	<1
Mn (ppb)	<1	<1
Fe (ppm)	<0.01	<0.01
Ni (ppb)	2.60	<1
Cu (ppb)	<1	<1
Zn (ppb)	1.52	<1
Cd (ppb)	<1	<1
Sn (ppb)	<1	<1
Sb (ppb)	<1	<1
Ba (ppb)	13.38	<1
Pb (ppb)	<1	<1
pH	8.28	-
Conductivity (μS/cm)	386	-

nd: not determined.

Table 3. Major dissolved cation and anion concentrations in the tap water as determined by IC analysis.

Cations (ppm)			
Na^+	K^+	Mg^{++}	Ca^{++}
18.9	0.62	11.8	59.5
Anions (ppm)			
F^-	Cl^-	NO_3^-	SO_4^{2-}
0.1	15.2	2.8	15.9

experimentally documented low-temperature aragonite growth (Fernández-Díaz et al., 1996; Zhang and Dawe, 2000; De Choudens-Sánchez and González, 2009). Furthermore, their upward-directed terminal tips suggest relatively unrestricted crystal growth within the boiling water column rather than exclusively by attachment to previously deposited carbonate surfaces. Although these morphological characteristics strongly support an aragonite interpretation, the mineralogical identification of individual crystals is based on the combined evidence provided by XRD, FTIR, Raman spectroscopy, SEM morphology, and EDX microchemistry.

Raman spectroscopy independently corroborates the coexistence of calcite and aragonite established by XRD and FTIR, consistent with the characteristic Raman features reported for carbonate minerals (Edwards et al., 2005; Alves et al., 2023). The Raman spectra obtained from the different morphologies are broadly similar because the analyzed domains commonly comprise intimate intergrowths of carbonate phases within the approximately 1 μm laser spot. Consequently, Raman spectroscopy was used primarily as a qualitative technique to support the mineralogical interpretation rather than for quantitative estimation of calcite/aragonite proportions. The assignment of calcite-dominant and aragonite-dominant morphologies is therefore based on the integrated interpretation of the Raman spectra together with the XRD, FTIR, SEM crystal morphology, and SEM-EDX data.

Rosette-like aggregates, cauliflower-like aggregates, hexagonal plates, and poorly ordered carbonate material (POC) represent compositionally distinct late-stage precipitates formed under highly evolved evaporative conditions. Their elevated Mg and Si contents together with reduced Ca concentrations exceed the substitution limits generally reported for crystalline calcite and aragonite and therefore suggest the presence of chemically distinct Mg-rich poorly ordered carbonate material, which may include Mg-stabilized amorphous calcium carbonate (ACC) or related transitional phases (Chakrabarty and Mahapatra, 1999; Chen et al., 2020). Their nanogranular textures and preferential occurrence near the uppermost parts of the deposits further indicate precipitation from highly evolved residual solutions. Rapid evaporation of the remaining water film likely promoted Mg and Si enrichment, inhibited complete crystallization, and favored the preservation of these poorly ordered carbonate products. The coexistence of crystalline aragonite with these Mg-rich phases suggests that carbonate precipitation remained active throughout the boiling cycle under progressively evolving physicochemical conditions.

XRD identified only crystalline aragonite and calcite, whereas the elevated Mg and Si contents observed in several irregular morphologies indicate the presence of poorly ordered or amorphous carbonate material that is not readily detected by conventional XRD. Because no internal standard was included in the XRD analysis, the abundance of any amorphous component could not be quantified.

Consequently, the interpretation of these materials relies primarily on their microchemical composition, Raman characteristics, and textural relationships rather than on direct mineralogical identification.

Overall, no single analytical technique provides definitive identification of all carbonate morphologies. Instead, the proposed precipitation sequence and phase-morphology relationships are supported by the integrated interpretation of XRD, FTIR, Raman spectroscopy, SEM observations, and EDX microchemistry. Collectively, these complementary datasets support a coherent model involving early calcite nucleation, subsequent aragonite overgrowth during sustained boiling, and the late-stage formation of Mg-Si-rich poorly ordered carbonate material under near-dry evaporative conditions.

CONCLUSIONS

The integrated mineralogical, micromorphological, spectroscopic, and geochemical analyses demonstrate that kettle limescale from Mersin formed through a multistage sequence of low-temperature $CaCO_3$ precipitation controlled by progressive heating, evolving solution chemistry, CO_2 degassing, and evaporation. The combined evidence from XRD, FTIR, Raman spectroscopy, SEM observations, and EDX microchemical data indicates that rod-shaped needles and small rhombohedral crystals represent the earliest stage of scale formation. In contrast, elongated pseudo-hexagonal prismatic crystals subsequently overgrew these early carbonate phases during continued boiling, reflecting a sequential crystal-growth process.

Rosette-like and cauliflower-like aggregates, hexagonal plates, and poorly ordered carbonate material (POC) are characterized by enrichment in Mg and Si together with depletion in Ca relative to the dominant crystalline carbonate morphologies, indicating compositionally distinct late-stage precipitates formed under highly evolved evaporative conditions. Although Raman spectroscopy independently confirms the coexistence of calcite and aragonite, the mineralogical interpretation of individual morphologies is based on the integrated evaluation of Raman spectra together with XRD, FTIR, SEM crystal morphology, and SEM-EDX data rather than on Raman spectroscopy alone.

The hydrochemical composition of the tap water, controlled by the ophiolitic, evaporitic, and carbonate lithologies of the Berdan Dam catchment, provided favorable physicochemical conditions for carbonate precipitation and influenced carbonate polymorphism, crystal morphology, and elemental partitioning during repeated boiling. Overall, kettle limescale represents a useful natural analogue for low-temperature carbonate precipitation and demonstrates how progressive heating, CO_2 degassing, evolving water chemistry, and evaporation collectively govern carbonate polymorphism, crystal growth, and the development of complex carbonate microtextures in near-surface environments.

ACKNOWLEDGEMENTS

The second author of this article, Prof. Dr. Selahattin Kadir, who contributed to the study, has passed away. This paper is dedicated to his memory.

REFERENCES

Abdelghani H., Ahmed A., Abdellah E.B., 2018. The Impact of Limescale on Home Appliances in a Building. In Proceedings of the 1st International Conference of Computer Science and Renewable Energies Volume 1, 423-428.

Al-Gailani A., Charpentier T.V.J., Sanni O., Neville A., 2022. Crystallization Fouling in Domestic Appliances and Systems. Heat Transfer Engineering 43, 301-310.

Alves J.F., Edwards H.G., Korsakov A., De Oliveira L.F.C., 2023. Revisiting the Raman spectra of carbonate minerals. Minerals 13, 1358.

Belattar M., Ben-Aazza S., Aba-Aaki R., Hadfi A., Hafid N., Boukbir L., Driouiche A., 2016. Contribution to the study of hot water scaling phenomenon in the south of touristic area in Agadir City. Journal of Water Resource and Protection 8, 1035-1043.

Brindley G.W., 1980. Quantitative X-ray analysis of clays. In: Crystal Structures of Clay Minerals and their X-ray Identification (Mineralogical Society Monograph No. 5). (Eds.): G.W. Brindley, G. Brown, London (England), 411-438.

Burton E.A. and Walter L.M., 1987. Relative precipitation rates of aragonite and Mg calcite from seawater: Temperature or carbonate ion control? Geology 15, 111-114.

Butler J.C., 1975. Tea kettle carbonates. Journal of Sedimentary Petrology 45, 891-893.

Chakrabarty D. and Mahapatra S., 1999. Aragonite crystals with unconventional morphologies. Journal of Materials Chemistry 9, 2953-2957.

Chen Q., Ding W., Peng T., Sun H., 2020. Synthesis and characterization of calcium carbonate whisker from yellow phosphorus slag. Open Chemistry 18, 347-356.

De Choudens-Sánchez V. and González L.A., 2009. Calcite and aragonite precipitation under controlled instantaneous supersaturation: elucidating the role of $CaCO_3$ saturation state and Mg/Ca ratio on calcium carbonate polymorphism. Journal of Sedimentary Research 79, 363-376.

Edwards H.G., Villar S.E.J., Jehlicka J., Munshi T., 2005. FT-Raman spectroscopic study of calcium-rich and magnesium-rich carbonate minerals. Spectrochimica Acta Part A: Molecular and Biomolecular Spectroscopy 61, 2273-2280.

Fernández-Diaz L., Putnis A., Prieto M., Putnis C.V., 1996. The role of magnesium in the crystallization of calcite and

aragonite in a porous medium. Journal of Sedimentary Research 66, 482-491.

Gray N.F., 2008. Drinking water quality: problems and solutions, 2nd edition. Cambridge University Press, Cambridge, 538 pp.

Hafid N., Belattar M., Ben-Aazza S., Hadfi A., Ezahri M., Driouiche A., 2015. Characterization of scale formed in drinking water and hot water pipes in the Taliouine Downtown-Morocco. American Journal of Analytical Chemistry 6, 677-686.

Hanifa M., Sharma U., Thapliyal P.C., Singh L.P., 2025. Effects of temperature, pH and calcium-to-carbonate ratio on the calcium carbonate polymorphs. Discover Civil Engineering 2, 147.

Itoh N., 2026. Reliable Estimation of Wavenumbers for Calcite Peaks. Journal of Raman Spectroscopy 57, 821-827.

Kapur S., Akça E., Kadir S., Previtali F., Billor Z., Zucca C., Casati E., Eren M., Karagöz A., Nazik A. et al., 2025. Pedogenic evidence sheds light on the post-Roman pedo-sedimentological and human history of Tarsus, the Roman capital of CE 60, Cilicia, Mersin, Türkiye. Catena 248, 108544.

Kontoyannis C.G. and Vagenas N.V., 2000. Calcium carbonate phase analysis using XRD and FT-Raman spectroscopy. Analyst 125, 251-255.

Liendo F., Arduino M., Deorsola F.A., Bensaid S., 2022. Factors controlling and influencing polymorphism, morphology, and size of calcium carbonate synthesized through the carbonation route: A review. Powder Technology 398, 117050.

Martínez Moya S. and Boluda Botella N., 2021. Review of techniques to reduce and prevent carbonate scale. Prospecting in water treatment by magnetism and electromagnetism. Water 13, 2365.

Moore D.M. and Reynolds R.C., 1989. X-ray Diffraction and the Identification and Analysis of Clay Minerals. Oxford University Press, Oxford, 332 pp.

Van der Marel H.W. and Beutelspacher H., 1976. Atlas of IR Spectroscopy of Clay Minerals and Their Admixtures, Elsevier, Amsterdam, 396 pp.

Wray J.L. and Danniels F., 1957. Precipitation of calcite and aragonite. Journal of the American Chemical Society 79, 2031-2034.

Yetiş C., Kelling G., Gökçen S.L., Baroz F., 1995. A revised stratigraphic framework for later Cenozoic sequences in the northeastern Mediterranean region. Geologishe Rundschau 84, 794-812.

Zhang Y. and Dawe R.A., 2000. Influence of Mg^{2+} on the kinetics of calcite precipitation and calcite crystal morphology. Chemical Geology 163, 129-138.

This work is licensed under a Creative Commons Attribution 4.0 International License CC BY-NC-SA